processes

MDPI

Article

Thermal Swing Reduction-Oxidation of Me(Ba, Ca, or Mg)SrCoCu Perovskites for Oxygen Separation from Air

Julius Motuzas [1,*], Shaomin Liu [2] and João C. Diniz da Costa [1,3,4]

[1] FIM²Lab—Functional and Interfacial Materials and Membranes Laboratory, School of Chemical Engineering, The University of Queensland, St. Lucia, QLD 4072, Australia
[2] State Key Laboratory of Organic-Inorganic Composites, College of Chemical Engineering, Beijing University of Chemical Technology, Beijing 100029, China
[3] LAQV-REQUIMTE, (Bio)Chemical Process Engineering, Department of Chemistry, Faculty of Science and Technology, Universidade NOVA de Lisboa, 2829-516 Caparica, Portugal
[4] iBET—Instituto de Biologia Experimental e Tecnológica, 2781-901 Oeiras, Portugal
* Correspondence: j.motuzas@uq.edu.au; Tel.: +61-7-3365-8835; Fax: +61-7-3365-4199

Abstract: The climate change impact associated with greenhouse gas emissions is a major global concern. This work investigates perovskite compounds for oxygen separation from air to supply oxygen to oxyfuel energy systems to abate these significant environmental impacts. The perovskites studied were $Me_{0.5}Sr_{0.5}Co_{0.8}Cu_{0.2}O_{3-\delta}$ (MeSCC) where the A-site substitution was carried out by four different cations (Me = Ca, Mg, Sr, or Ba). SEM analysis showed the formation of small particle (<1 µm) aggregates with varying morphological features. XRD analysis confirmed that all compounds were perovskites with a hexagonal phase. Under reduction and oxidation reactions (redox), Ba and Ca substitutions resulted in the highest and lowest oxygen release, respectively. In terms of real application for oxygen separation from air, Ba substitution as BaSCC proved to be preferable due to short temperature cycles for the uptake and release of oxygen of 134 °C, contrary to Ca substitution with long and undesirable temperature cycles of 237 °C. As a result, a small air separation unit of 0.66 m^3, containing 1000 kg of BaSCC, can produce 18.5 ton y^{-1} of pure oxygen by using a conservative heating rate of 1 °C min^{-1}. By increasing the heating rate by a further 1 °C min^{-1}, the oxygen production almost doubled by 16.7 ton y^{-1}. These results strongly suggest the major advantages of short thermal cycles as novel designs for air separation. BaSCC was stable under 22 thermal cycles, and coupled with oxygen production, demonstrates the potential of this technology for oxyfuel energy systems to reduce the emission of greenhouse gases.

Keywords: oxygen; oxyfuel; perovskite; carbon capture

Citation: Motuzas, J.; Liu, S.; da Costa, J.C.D. Thermal Swing Reduction-Oxidation of Me(Ba, Ca, or Mg)SrCoCu Perovskites for Oxygen Separation from Air. *Processes* **2022**, *10*, 2239. https://doi.org/10.3390/pr10112239

Academic Editor: Wei-Hsin Chen

Received: 21 July 2022
Accepted: 20 October 2022
Published: 1 November 2022

1. Introduction

The recent 2021 Intergovernmental Panel on Climate Change (IPCC) report [1] has given a code red to humanity due to the continuous and increasing CO_2 emissions worldwide. These emissions are directly associated with the use of fossil fuels in energy and transportation, leading to climate change. Evidence of climate change is mounting with major and serious environmental events in 2021 such as wildfires in the USA, Canada, Turkey, Greece, and Italy, in addition to the unprecedented damage caused by floods in both Germany and Belgium. Hence, there is an immediate need to start reducing CO_2 emissions to abate the deleterious global effect of climate change.

The problem here is that our contemporary society is highly dependent on energy systems that maintain jobs, social stability, economic growth, and our quality of life. Our current energy needs are provided by fossil fuels (84%) and renewable resources (16%; e.g., mainly, hydro, solar, and wind powers) [2]. As our main energy needs are likely to be dependent upon fossil fuels for the foreseeable future to maintain world stability, our society has greater responsibilities to avert climate change for the sake of future

generations. In terms of energy production systems, one feasible approach is carbon capture from coal power generation plants followed by pure CO_2 pipeline transportation for storage in stable underground geological formations [3–5]. One approach of great interest is oxyfuel coal combustion that leads to the production of almost pure CO_2 [6–8]. Advances in oxyfuel combustion are directly associated with materials improvement as oxygen carriers in chemical looping process [9–12], many of which are perovskite-type materials [13,14], or using perovskites for oxygen separation in thermal redox cycling process or as membranes [15,16].

Perovskite compounds containing metal oxides (i.e., Ba, La, Sr, Co, Fe, Cu, Ca, Zn, Zr, and Y among others) [17–28] have been widely reported for oxygen separation from air. These compounds have been extensively used to prepare perovskite membranes and optimised to deliver high oxygen fluxes [29–32]. Membrane systems are advantageous as they offer continuous operation. However, perovskite membranes operate at very high temperatures (~900 °C), and sealing engineering solutions are complex and expensive. To avoid sealing problems, perovskites can also be prepared as powders to separate oxygen from air in batch processes [33–35]. These are similar to thermal swing sorption processes via the redox reaction, whereby oxygen is released (reduction) at the high temperature point and sorbed (oxidation) at the low temperature point. Under redox cycling, perovskites undergo a series of thermochemical and structural changes to separate oxygen from air.

Perovskites are an interesting and special type of ceramic material. Perovskites are crystalline materials containing two cation sites (A and B) and defined by the general formula ABO_3 [36,37]. The cation sites A and B are generally constituted of rare earth and alkaline elements, respectively. Teraoka et al. [38] demonstrated that the perovskite structure can be optimised in terms of oxygen vacancy defect concentration by adding other cations (A′ or B′) of different sizes and valences, thus creating perovskite crystal with a general formula $A_xA'_{1-x}B_yB'_{1-y}O_{3-\delta}$. However, the mixing of cations to be effective in forming perovskite crystalline structures must meet the tolerance factor (t), also known as the Goldschmidt number [39].

Lin's group reported a series of SrCoFe oxides and perovskite in thermal swing redox cycling [40,41]. Although these materials separated oxygen from air, the oxygen production was hampered by very low oxygen desorption rates. However, by substituting La in the A-site, and forming LaSrCoFe perovskites, Lin's group demonstrated that the redox cycles reduced, and oxygen production increased to 1.2 wt% per unit mass of LaSrCoFe [42]. Based on these promising results, there is an array of perovskite compounds that can be developed for the purpose of separating oxygen from atmospheric air by thermal swing redox processing. Provided that the Goldschmidt tolerance factor is met, there are numerous cations that can be substituted in A- and B-sites. The engineering considerations of these materials are those related to oxygen uptake/release per unit mass of the sorbent and shorter redox temperature range. By coupling these two engineering parameters, high oxygen production can be achieved as shorter redox temperature range implies that the redox cycle can be repeated more often.

There are numerous potential perovskite candidates that could meet the required engineering oxygen production. The most obvious candidate is BaSrCoFe (BSCF), one of the most studied perovskite materials used for oxygen separation from air in membrane systems [43]. However, Leo et al. [44] reported that the substitution of Fe with Cu in the B-side led to the formation of a new compound BaSrCoCu (BSCC) where oxygen fluxes more than doubled as compared to BSCF. Indeed, Cu based oxides are promising materials for oxygen storage. For instance, Motuzas et al. [45] showed that Cu in CuCo binary oxides increased the oxygen exchange in Co, leading to 5.0 wt% oxygen uptake. Subsequently, Vieten et al. [46] reported that that SrFeCu perovskites reached 2 wt% oxygen uptake, superior than many other perovskite compounds tested, such as CaSrMn at thermal cycle of 400 to 1000 °C. Therefore, Cu-based oxides and perovskites proved to deliver best performance in membranes and in thermal swing redox processes. Although there is stronger evidence from literature that quartenary perovskite membranes deliver

the highest oxygen fluxes, previous studies for thermal swing redox process were limited to binary oxides or ternary perovskite compounds.

Therefore, this work investigates the effect of quartenary perovskite compounds for oxygen separation from air. Cu-based perovskites were selected in view of their best proven performance reported in literature. This work focuses particularly on the A-site substitution of SrCoCu (SCC) perovskites with other metal cation (Me = Ba, Ca and Mg), thus forming a quartenary perovskite compound, MeSCC. The influence of A-site metal cation substitution is addressed in terms of materials properties and oxygen exchange (uptake and release) in a range of temperatures and redox cycling. Furthermore, the performance of the MeSCC compounds is assessed in terms of oxygen production by taking into consideration oxygen uptake and cycling time.

2. Materials and Methods

All chemicals used in this work were purchased from AlfaAesar and used as received, including $Cu(NO_3)_2 2.5H_2O$, $Co(NO_3)_2 6H_2O$, $Sr(NO_3)_2$, $Ca(NO_3)_2 4H_2O$, $Mg(NO_3)_2 6H_2O$, $Ba(NO_3)_2$, ethylenediamine tetraacetic acid (EDTA), and citric acid. All samples were prepared by using a modified Pechini method and based on the general formula $Me_{0.5}Sr_{0.5}Co_{0.8}Cu_{0.2}O_{3-d}$, where the cation Me represents Ca, Mg, Sr, or Ba. Initially, the precursor chemicals were mixed prior to the addition of citric acid. Subsequently, the resultant mixture was dissolved in water followed by the addition of EDTA to the solution, forming a sol. Under constant stirring, ammonia (32 wt% in water) was added to the sol until EDTA was completely dissolved. The clear solution was heated to 120 °C and left under stirring until a viscous fluid was formed. To complete the evaporation, the fluid was transferred to an oven for 12 h at 200 °C. Upon drying, the resultant solid was initially calcined at 450 °C with a dwell time of 4 h in air to burn any organics. This was followed by a second calcination step at 1000 °C for 4 h in air to decompose carbonates and leading to the formation of perovskite structures. The resultant perovskites $Me_{0.5}Sr_{0.5}Co_{0.8}Cu_{0.2}O_{3-\delta}$ (MeSCC) were named MgSCC, CaSCC, and BaSCC depending on the cation substitution in the A-site of the perovskite crystal. A blank sample SrSCC containing Sr in the A-site only as a ternary perovskite compound was also prepared and tested for comparison purposes with the other quartenary MeSCC perovskite compounds.

The diffraction patterns of the resultant powders were measured by using a Rigaku SmartLab X-ray Diffractometer equipped with 9 kW rotating (Cu) anode X-ray generator operating at 45 kV and 200 mA by step scanning in the range of $10 \leq 2\theta \leq 100°$. The recorded XRD patterns were compared and cell parameters calculated by using DIFFRAC.SUITE EVA software. The oxygen exchange was analyzed from 25 to 1000 °C at a rate of 5, 10 and 20 °C min^{-1} in air by using a thermogravimetric analyzer (TGA/DSC 1, Mettler-Toledo). The air feed flow rate was set as a constant at 80 mL min^{-1} for all measurements. The morphological features of the perovskite samples were examined by using a Jeol JSM-7001F SEM with a hot (Schottky) electron gun at an accelerated voltage of 5 kV.

3. Results and Discussion

Figure 1 shows representative SEM images of sintered samples, which display similar particle features. For instance, small particles (<1 μm) coalesced forming necks, attributed to the sintering effect at high temperatures. However, different morphological features are observed. The magnesium substituted material was composed of clusters of small particles (Figure 1a), whereas the calcium analog displayed a layered structure containing several particles (Figure 1b). The strontium-substituted perovskite resulted in longer thin shape particles of intergrown network (Figure 1c). Finally, the barium analog yielded larger aggregates of sintered particles (Figure 1d).

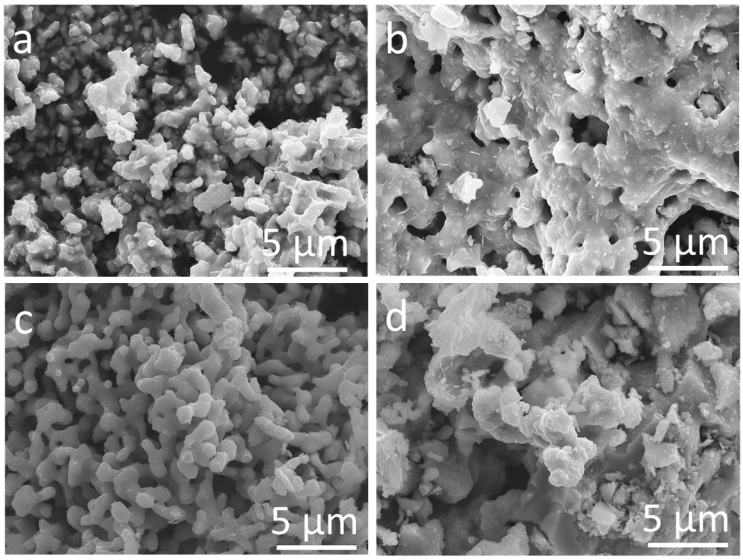

Figure 1. SEM images of $Me_{0.5}Sr_{0.5}Co_{0.8}Cu_{0.2}O_{3-\delta}$ where Me is Mg (**a**), Ca (**b**), Sr (**c**), Ba (**d**).

Figure 2 exhibits the XRD patterns of MeSCC samples. These patterns contain multiple peaks with the major diffractions at 2θ 18.52 [001], 28.44 [020], 32.52 [211], 36.62 [310], 42.61 [030], 43.79 [202], 46.58 [212], 55.61 [330], 61.79 [041], 68.23 [422], 74.12 [601], 75.55 [050] and 78.01 [620] [(PDF #00-040-1018) for magnesium; 18.75 [110], 29.33 [115], 32.48 [300], 36.56 [121], 40.46 [223], 42.53 [208], 43.59 [217], 44.70 [225], 46.34 [218], 57.1 [318], 62.04 [423], 69.71 [427], 73.93 [115] and 77.94 [613] (PDF 00-060-0753) for calcium; 18.546 [110], 28.46 [113], 32.53 [300], 43.857 [006], 46.51 [125], 47.64 [116], 55.46 [306], 57.99 [045], 62.39 [235], 68.11 [505] and 75.47 [336] (PDF #04-015-9915) for strontium; and 19.95 [110], 26.71 [101], 31.11 [110], 41.48 [002], 44.11 [102], 52.83 [112], 54.37 [211], 65.25 [212], 71.46 [302], and 73.83 [311] (PDF #04-016-5545) for barium-containing materials. These patterns show the formation of perovskite compounds containing crystal phases. Furthermore, minor additional peaks at 36.54 [111], 42.61 [200], 62.06 [220], 73.89 [311], and 77.66 [220] corresponding to the CoO pattern (PDF #00-043-1004) were observed for the samples with magnesium and calcium. Therefore, all MeSCC samples confirm that the metal cation (Mg, Ca, Sr, and Ba) used was fully substituted in the A-site.

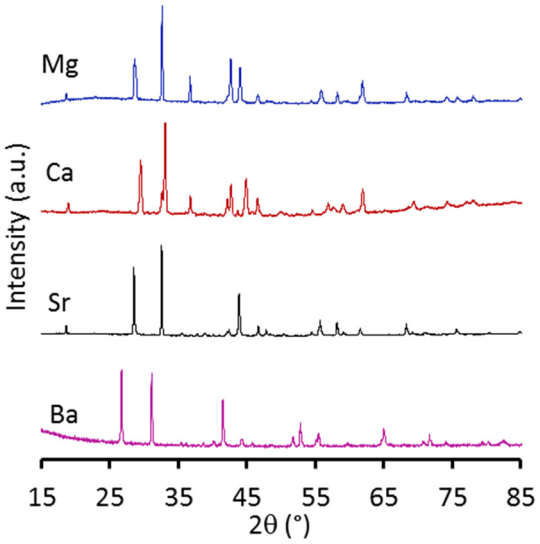

Figure 2. X-ray diffraction patterns of as prepared perovskite materials.

All samples were analysed by using Diffrac.Suite Eva software, and results are presented in Table 1. It is interesting to observe that results reveal the formation of a hexagonal

crystal phase consistent with reports elsewhere [47–49]. The Goldschmidt tolerance factor (t) varied depending on the Me substitution in the A side. For instance, Ba substitution resulted in a tolerance factor BaSCC (t = 1.04) higher than other compounds MgSCC (t = 0.89) CaSCC (t = 0.97), and SrSCC (t = 0.98). The unit cell parameters were also calculated as displayed in Table 1. It is interesting to note the trend in the volumes of the unit cell of the A-site substitution of Sr > Mg > Ca > Ba did not increase in the same fashion as the size of the ion radii Ba^{2+} (1.61 Å) > Sr^{2+} (1.44 Å) > Ca^{2+} (1.34 Å) > Mg^{2+} (0.89 Å). In this case, SrSCC is a blank sample for comparison purpose, as the A-site contains Sr ($Sr_{0.5}Sr_{0.5}Co_{0.8}Cu_{0.2}O_{3-\delta}$ equal to $Sr_{1.0}Co_{0.8}Cu_{0.2}O_{3-\delta}$) only, and not two cations as the other compounds.

Table 1. Calculated Goldschmidt tolerance factor (t) and unit cell parameters for lattice (a, b, c) and volume (V) of as-sintered perovskite compounds.

Compound	Calculated from Measurements					
	t	a (Å)	b (Å)	c (Å)	V (Å^3)	Crystal Structure
MgSCC	0.89	9.497	9.497	12.402	968.85	Hexagonal
CaSCC	0.95	9.08	9.08	10.32	736.9	Hexagonal
SrSCC	0.98	9.5	9.5	12.427	971.4	Hexagonal
BaSCC	1.04	5.591	5.591	4.28	115.9	Hexagonal

Figure 3 shows that the mass of all samples decreased as the temperature increased, attributed to the reduction of the MeSCC samples. This result implies that oxygen was desorbed (i.e., released) from the perovskite structure. The opposite trend occurred when the temperature decreased, as all samples increased in mass, thus gaining oxygen from air. This is associated with the oxidation reaction and known as sorption (i.e., uptake). Hence, these results confirmed the redox reactions of all perovskite samples as a function of the temperature. The total mass change of the MeSCC samples followed the trend of the Ba (1.72 wt%) > Sr (1.69 wt%) > Mg (1.41 wt%) > Ca (0.87 wt%). These results correlate well with Ba and Sr substitution in the A-site of perovskites. For instance, BaSrCoFe (BSCF) has been extensively studied owing to this compound excellent performance as perovskite membrane [50]. The highest performance of Ba and Sr A-site substation is a direct result of the redox effect, in line with the results observed in this work for MeSCC compounds.

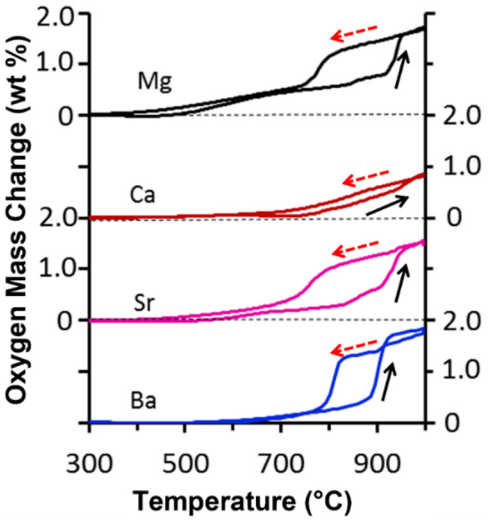

Figure 3. Oxygen sorption (broken arrow) and desorption (full arrow) as a function of temperature.

Figure 4a displays the redox cycle hysteresis of all samples as a function of temperature. These results clearly indicate different temperatures in terms of oxygen desorption as temperature increased and sorption with temperature decreased. For instance, the mass loss or desorption started at 400 °C (MgSCC), 452 °C (SrSCC), 522 °C (BaSCC), and

669 °C (CaSCC) until the final tested temperature of 1000 °C. However, the mass gain or sorption for CaSCC is comparatively smaller than that of the other tested perovskites as the temperature decreased from 1000 °C. All samples started gaining mass slowly, though there was a significant mass gain at both 775 °C (MgSCC and SrSCC) and 810 °C (BaSCC). These results are in line with Figure 3. The heat flow results in Figure 4b are consistent with the redox reactions. As the temperature increases, heat is provided for the oxygen release, confirming a reduction reaction which is endothermic. By the same token, as oxygen is absorbed, heat is released, thus giving an exothermic reaction. It is also observed that the endothermic peaks for the oxygen release have higher areas as Ba > Sr > Mg > Ca. This trend follows the mass uptake in Figure 3 as Ba > Sr > Mg > Ca and confirms that more energy is required as the MeSCC releases more oxygen from their structure.

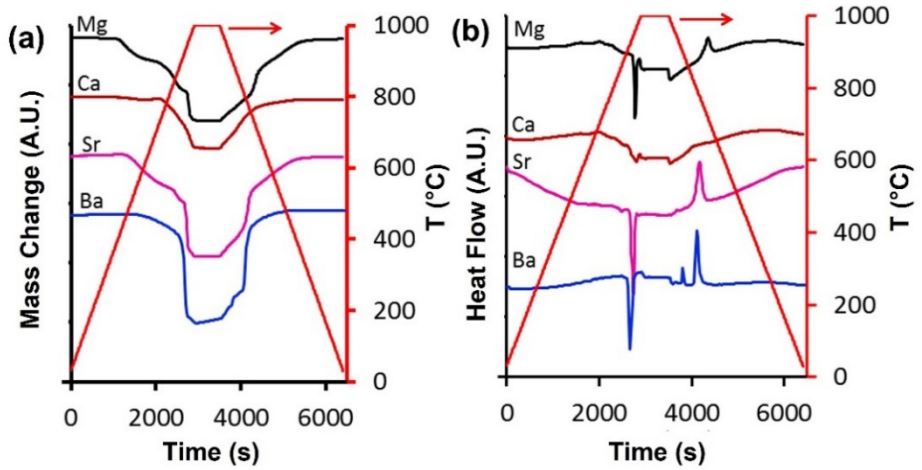

Figure 4. Comparison of the performance of MeSCC. (**a**) Oxygen sorption/desorption and (**b**) heat flow as a function of time at a heating/cooling rate of 20 °C min^{-1}.

The results in Figure 4 fundamentally reflect the mechanism of oxygen separation from air that is well known for perovskite materials described by Equation (1) as follows:

$$ABO_{3-A\ (oxidation)}(Low\ Temp) \leftrightarrow ABO_{3-B\ (reduction)}(High\ Temp) + 0.5(B-A)O_2 \quad (1)$$

where A and B are the two cation sites of the perovskite crystal materials, and O is the oxygen molecule. At low temperature, oxygen ions are incorporated or sorbed into the crystal structure, also known as oxidation. At high temperatures, oxygen ions are released or desorbed from the crystal structure and combine at the surface of the particle to form O_2 molecule, in a process called reduction. This redox process is modulated by oxygen ions and differs completely from molecular gas separation by size exclusion in membranes based on porous crystals [51] and amorphous silica [52], or molecular gas sorption/desorption in the pressure swing adsorption (PSA) process using solid sorbents [53] or amine-functionalised solid sorbents [54].

In terms of engineering application, these results beg the question of which of the above MeSCC samples has the best prospect for separating oxygen from air. Let us consider a simplified process flow diagram in Figure 5 containing a vessel (adsorbent bed with MeSCC) for oxygen separation from air. This process works under a redox cycle. In the oxidation cycle, the adsorbent bed is at the highest temperature set point, so the hot air feeding reduces the temperature of the vessel and leads to oxygen absorption by MeSCC. An added benefit here is that as oxygen absorbs, high concentration nitrogen gas exits the vessel, which can be sold as a feedstock to other industrial applications. In the reduction cycle, the vessel at the low temperature set point is initially emptied of any non-absorbed gas. Subsequently, the temperature is increased to the high temperature set point when the oxygen is released from the MeSCC sorbent and exits the vessel accordingly. Then the redox cycles are repeated. In terms of industrial application, this simplified process will require

CO_2 guard bed and water-drying units prior to pure dry feed air entering the column for O_2 and N_2 separation. CO_2 and H_2O are detrimental to perovskites, resulting in loss of performance. CO_2 reacts of oxides in perovskite materials resulting in carbonation [55], and CO_2 and water as steam accelerates leaching of perovskite compounds [56].

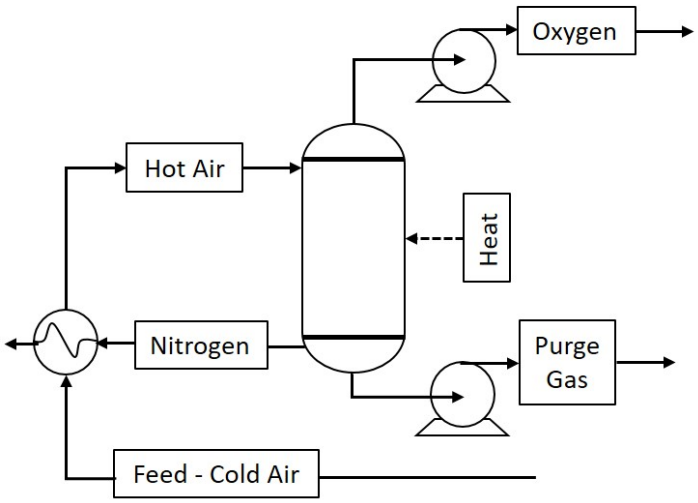

Figure 5. Thermal swing redox process flow diagram.

The redox cycling in Figure 5 can be deducted from simple engineering principles of mass balance. It consists of an oxidation cycle (*ox*), on reduction cycle (*red*) and two idle cycles to equilibrate the column conditions between the cycles of *ox/red* and *red/ox*. The calculation of the annual production of oxygen (P_{ox}) was carried out on the engineering basis of 1000 kg mass of sorbent MeSCC (m_{sorb}) for the percentage of O_2 mass sorbed/desorbed ($m_{ox\%}$) and the number of redox cycles per year ($C_{n,y}$) as in Equation (2):

$$P_{ox} = m_{sorb} m_{ox\%} C_{n,y} \tag{2}$$

The number of redox cycles per year ($C_{n,y}$) can be determined by using Equation (2):

$$C_{n,y} = \frac{1}{t_{n,y}} \tag{3}$$

and the time taken for each cycle t_c can be calculated as per Equation (4) and normalized from cycles per min to the total number of cycles for a full year as $t_{n,y}$:

$$t_c = \frac{\Delta T_{sorp}}{h_{sorp}} + \frac{\Delta T_{des}}{h_{des}} + 2t_{eq} \tag{4}$$

where h is the heating rate (°C min^{-1}) and ΔT is the temperature range (°C) between sorption (i.e., oxidation) and desorption (i.e., reduction), and t_{eq} is the time (min) taken to equilibrate and switch the redox cycles. For this calculation, the heating rate was set at 1 °C min^{-1}, a conservative assumption, instead of 20 °C min^{-1} as used in this experimental laboratory work. Furthermore, there is a need to equilibrate the operating conditions (i.e., temperature, fill and/or empty vessel) of the adsorption bed each time that the cycle changes from reduction to oxidation and from oxidation back to reduction and so forth.

Hence, a reasonable time of 5 min was allocated for each cycle change. Another important parameter for this calculation is the time taken by each MeSCC for both oxidation and reduction reactions. In order to optimise the production of oxygen, the low- and high-temperature set points were taken from Figure 4a where the oxygen sorption or desorption changed from their highest to the lowest values. Therefore, the calculations of the annual production of oxygen were carried out by using the values set out in Table 2.

Table 2. Oxygen sorption/desorption (wt%) and redox temperature cycle (ΔT) for the standard full cycle (Figure 4) and optimised short cycle (see Figure S1 in Supplementary Information).

	Standard Full Cycle		Optimised Short Cycle	
MeSCC	***m* (wt%)**	**ΔT (°C)**	***m* (wt%)**	**ΔT (°C)**
Ba	1.72	478	0.98	134
Sr	1.69	548	0.76	235
Mg	1.41	600	0.67	187
Ca	0.87	331	0.47	237

Figure 6 shows the oxygen annual production for all samples for the standard values versus optimised values using Equations (2) and (3), and the parameters as per Table 2. It is interesting to see how effective the optimised results for BaSCC were. They almost doubled in oxygen production from 9.4 to 18.5 ton y^{-1}, and likewise the second-best oxygen production (MgSCC). In fact, the optimised cycle for BaSCC demonstrates the effectiveness of short-time batch cycles, which was aided by significant increases in oxygen sorption/desorption within a short redox temperature range (see calculations in Supplementary Information). The other samples had a relative longer redox temperature range for the optimised cycle and did not show significant variation in oxygen production as compared to the standard cycle. This was attributed to the trade-off due to lower oxygen sorption/desorption for optimised cycles. It is interesting to observe that MgSCC had the lowest standard oxygen production, although it had higher optimised oxygen production than SrSCC and CaSCC. This was associated with the fact that MgSCC had a shorter redox temperature cycle than the other two samples.

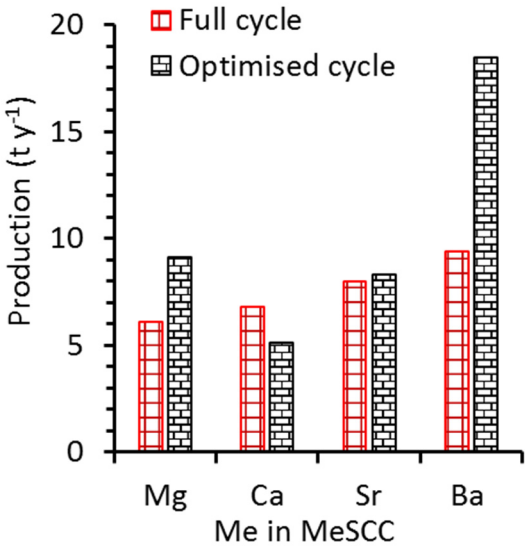

Figure 6. Annual oxygen production (t y^{-1}) using values from Table 2 and a heating/cooling rate of 1 °C min^{-1} and optimized conditions as a function of heating/cooling rates (See Figure S1 and calculations in Supplementary Information). Condition: sorbent column equilibration time of 5 min for each reduction and oxidation.

The best-performing BaSCC sample was further exposed to 30 redox cycles. Figure 7a clearly shows that BaSCC was stable during redox cycling thus confirming the potential of this material for oxygen separation from air. Further optimisation was carried out by increasing the heating rate for each redox cycle. Results in Figure 7b shows a fitting line (y = 16.7x), thus indicating that each time that the redox heating rates is raised by 1 °C min^{-1}, the annual oxygen production increased by 16.7 tonnes. In other words, increasing the column heating/cooling rates reduces the time required for the redox reactions, thus reflecting in significant oxygen annual production increase. These calculations were carried out on a basis of 1000 kg of BaSCC material. By taking into consideration an av-

erage BSCC density of 5810 kg m^{-3} and a free volume of 50% between pellets/particles, the column with 1000 kg of BaSCC sorbent bed will require a total volume of 0.66 m^3. Potentially, there are major capital cost savings by adopting BaSCC due to the column size being relatively small whereas other ancillary equipment, such as gas compressors to pressurise atmospheric air into the column, are not required as per the process flow diagram (Figure 5). Heating rate is also a critical parameter for the redox cycling. Figure 7b shows that the annual oxygen production increases linearly as a function of the heating rate. By doubling the heating rate, the redox cycle halves as per Equation (3), thus explaining that oxygen production increased twofold. These results can form the basis for scale-up rules, although process engineering design including complex heat exchange recovery and capital and economic cost analysis can be used to optimize the final design.

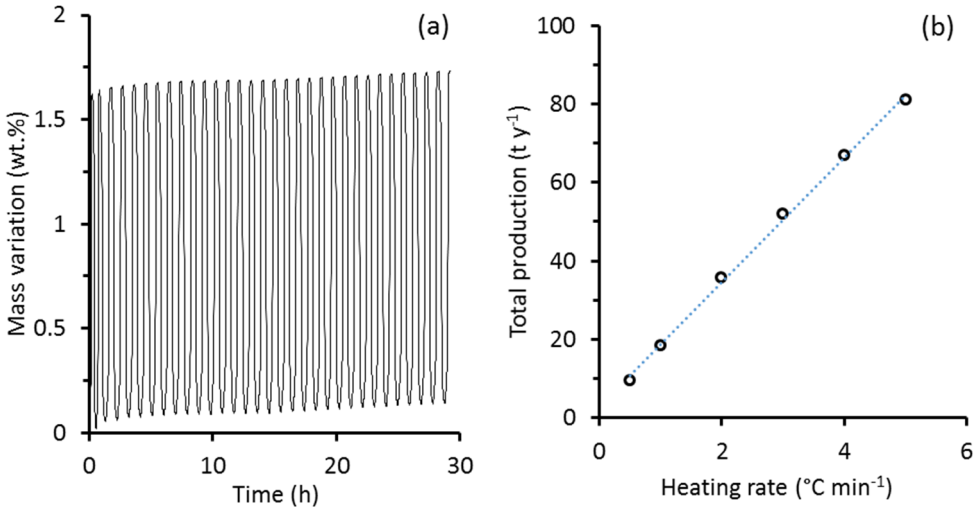

Figure 7. (**a**) BaSCC redox recycling between 720 and 960 °C at a heating rate of 20 °C min^{-1}, and (**b**) BaSCC annual oxygen production as a function of the heating and cooling rate of the column with BaSCC sorbent.

Figure 8a shows the O_2 mass desorbed from perovskites reported in literature. The BaSrCoCu in this work performed well with the seventh-best of ten results. However, this paper shows that short redox cycles are preferable giving the highest O_2 production instead of full cycles with the largest temperature changes. Not all the results in Figure 8a are available showing TGA redox cycling. Therefore, Figure 8b attempts to provide a fair comparison for results available in literature as the ratio of mass change over temperature change. A higher ratio is preferable, meaning that more mass of O_2 is produced per 1 °C of temperature change. The best material in this work BaSrCoCu performed well against other perovskites second to an optimized BaCoFe* only. Therefore, BaSrCoCu can be further optimized by changing the compositions of the A and B sites in order to deliver even higher performance.

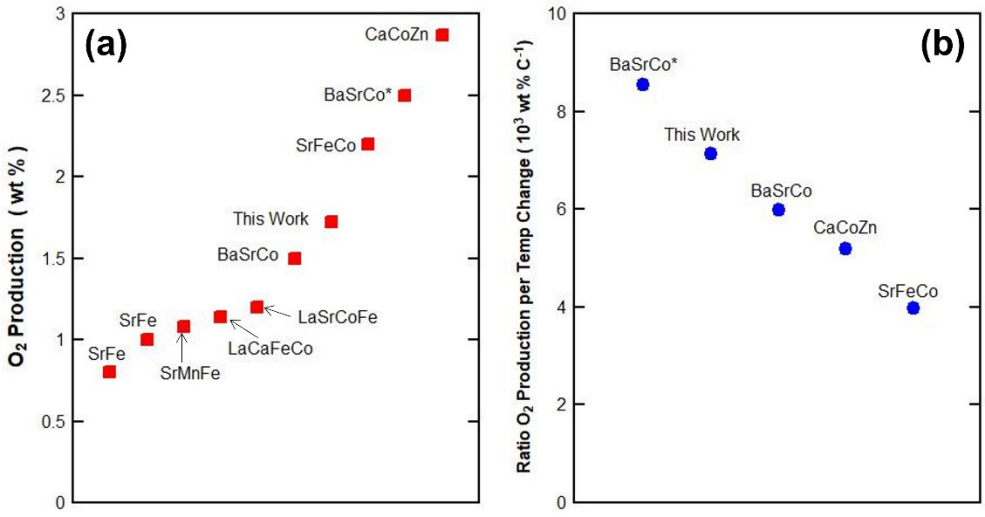

Figure 8. (**a**) Comparison of perovskite performance of O_2 production (wt%) as in this work BaSrCoCu, SrFe [14], SrFe [14], SrMnFe [12], LaCaFeCo [57], LaSrCoFe [42], BaSrCo, and improved BaSrCo* [58], SrFeCo [59] and CaCoZn [60]. (**b**) Comparison of perovskite performance as the ratio of O_2 production per temperature change (wt% C^{-1}) as in this work BaSrCoCu, BaSrCo and improved BaSrCo* based on optimized short redox cycles, and CaCoZn and SrFeCo based on desorption temperature information only as redox cycles were not given.

4. Conclusions

This work shows that the Ba substitution in MeSCC perovskite compounds resulted in the highest oxygen mass production under redox reactions. In addition, BaSCC exhibited the shortest redox thermal cycling, a major advantage as oxygen production rates increased, doubling as compared with the other MeSCC perovskites containing Mg, Ca, and Sr. BaSCC also proved to be stable. The combination of these important parameters has potential for novel engineering systems and shows that BaSCC adsorbent vessels can be relatively small with great capacity for oxygen separation from air. As a result, BaSCC thermal cycling units have the potential to supply oxygen for oxyfuel combustion carbon capture systems to abate the emission of greenhouse gases and climate change.

Supplementary Materials: The following supporting information can be downloaded at: https://www.mdpi.com/article/10.3390/pr10112239/s1, Figure S1: Oxygen sorption and desorption as a function of temperature with optimized short cycles for oxygen separation from air. Redox cycling calculations are also reported in the same document.

Author Contributions: Conceptualization, J.M. and J.C.D.d.C.; methodology, J.M. and J.C.D.d.C.; validation, J.M. and J.C.D.d.C.; formal analysis, J.M., S.L. and J.C.D.d.C.; investigation, J.M., S.L. and J.C.D.d.C.; data curation, J.M., S.L. and J.C.D.d.C.; writing—original draft preparation, J.M.; writing—review and editing J.M., S.L. and J.C.D.d.C.; visualization, J.M. and J.C.D.d.C.; project administration, J.C.D.d.C. All authors have read and agreed to the published version of the manuscript.

Funding: This research was financially supported by the Visiting Fellowship (for João C. Diniz da Costa) by the Associate Laboratory for Green Chemistry—LAQV, financed by the Portuguese National Government funds from FCT/MCTES (UIDB/50006/2020) and the Fundamental Research Fund for the Central University (Buctrc202115) in China.

Acknowledgments: The authors acknowledge the facilities, and the scientific and technical assistance, of the Australian Microscopy & Microanalysis Research Facility at the Centre for Microscopy and Microanalysis, The University of Queensland.

Conflicts of Interest: The authors declare no conflict of interest.

References

1. IPCC. *Climate Change 2021: The Physical Science Basis. Contribution of Working Group I to the Sixth Assessment Report of the Intergovernmental Panel on Climate Change*; Masson-Delmotte, V., Zhai, P., Pirani, A., Connors, S.L., Péan, C., Berger, S., Caud, N., Chen, Y., Goldfarb, L., Gomis, M.I., et al., Eds.; Cambridge University Press: Cambridge, UK, 2021. Available online: https://www.ipcc.ch/report/ar6/wg1/#FullReport (accessed on 1 June 2022).
2. *Bp Statistical Review of World Energy*, 70th ed.; British Petroleum Co.: London, England, 2021. Available online: https://www.bp.com/content/dam/bp/business-sites/en/global/corporate/pdfs/energy-economics/statistical-review/bp-stats-review-2021-full-report.pdf (accessed on 30 June 2022).
3. IEA Greenhouse Gas R&D Programme, Storing CO_2 Underground. 2007. Available online: https://ieaghg.org/docs/general_publications/storingCO.pdf (accessed on 30 June 2022).
4. Smart, S.; Lin, C.X.C.; Ding, L.; Thambimuthu, K.; da Costa, J.C.D. Ceramic membranes for gas processing in coal gasification. *Energy Environ. Sci.* **2010**, *3*, 268–278. [CrossRef]
5. Paltsev, S.; Morris, J.; Kheshgi, H.; Herzog, H. Hard-to-Abate sectors: The role of industrial carbon capture and storage (CCS) in emission mitigation. *Appl. Energy* **2021**, *300*, 117322. [CrossRef]
6. Castillo, R. Thermodynamic analysis of a hard coal oxyfuel power plant with high temperature three-end membrane for air separation. *Appl. Energy* **2011**, *88*, 1480–1493. [CrossRef]
7. Wall, T.; Liu, Y.; Spero, C.; Elliott, L.; Khare, S.; Rathnam, R.; Zeenathal, F.; Moghtaderi, B.; Buhre, B.; Sheng, C.; et al. An overview on oxyfuel coal combustion—State of the art research and technology development. *Chem. Eng. Res. Des.* **2009**, *87*, 1003–1016. [CrossRef]
8. Stanger, R.; Wall, T.; Spörl, R.; Paneru, M.; Grathwohl, S.; Weidmann, M.; Scheffknecht, G.; McDonald, D.; Myöhänen, K.; Ritvanen, J.; et al. Stanley Santos, Oxyfuel combustion for CO2 capture in power plants. *Int. J. Greenh. Gas Control* **2015**, *40*, 55–125. [CrossRef]
9. Siriwardane, R.; Riley, J.; Benincosa, W.; Bayham, S.; Bobek, M.; Straub, D.; Weber, J. Development of $CuFeMnAlO_{4+\delta}$ oxygen carrier with high attrition resistance and 50-kWth methane/air chemical looping combustion tests. *Appl. Energy* **2021**, *286*, 116507. [CrossRef]
10. Jia, T.; Popczun, E.J.; Lekse, J.W.; Duan, Y. Effective Ca^{2+}-doping in $Sr_{1-x}Ca_xFeO_{3-\delta}$ oxygen carriers for chemical looping air separation: A theoretical and experimental investigation. *Appl. Energy* **2021**, *281*, 116040. [CrossRef]
11. Abuelgasim, S.; Wang, W.; Li, T.; Abdalazeez, A.; Xia, Z. The effect of alkali and alkaline earth metals oxides addition on oxygen uncoupling rate of copper-based oxygen carrier: A kinetic and experimental investigations. *Sep. Purif. Technol.* **2021**, *275*, 119176. [CrossRef]
12. Görke, R.H.; Marek, E.J.; Donat, F.; Scott, S.A. Reduction and oxidation behavior of strontium perovskites for chemical looping air separation. *Int. J. Greenh. Gas Control* **2020**, *94*, 102891. [CrossRef]
13. Ikeda, H.; Tsuchida, A.; Morita, J.; Miura, N. $SrCo_xFe_{1-x}O_{3-\delta}$ oxygen sorbent usable for high-temperature pressure-swing adsorption process operating at approximately 300 °C. *Ind. Eng. Chem. Res.* **2016**, *55*, 6501–6505. [CrossRef]
14. Bulfin, B.; Lapp, J.; Richter, S.; Gubàn, D.; Vieten, J.; Brendelberger, S.; Roeb, M.; Sattler, C. Air separation and selective oxygen pumping via temperature and pressure swing oxygen adsorption using a redox cycle of $SrFeO_3$ perovskite. *Chem. Eng. Sci.* **2019**, *203*, 68–75. [CrossRef]
15. Leo, A.; Liu, S.; da Costa, J.C.D. Development of mixed conducting membranes for clean coal energy delivery. *Int. J. Greenh. Gas Control* **2009**, *3*, 357–367. [CrossRef]
16. Chen, W.; Chen, C.-S.; Bouwmeester, H.J.M.; Nijmeijer, A.; Winnubst, L. Oxygen-selective membranes integrated with oxy-fuel combustion. *J. Membr. Sci.* **2014**, *463*, 166–172. [CrossRef]
17. Rachadel, P.L.; Motuzas, J.; Machado, R.A.F.; Hotza, D.; da Costa, J.C.D. Influence of porous structures on O_2 flux of BSCF asymmetric membranes. *Sep. Purif. Technol.* **2017**, *175*, 164–169. [CrossRef]
18. Serra, J.M.; Garcia-Fayos, J.; Baumann, S.; Schulze-Küppers, F.; Meulenberg, W.A. Oxygen permeation through tape-cast asymmetric all-$La_{0.6}Sr_{0.4}Co_{0.2}Fe_{0.8}O_{3-\delta}$ membranes. *J. Memb. Sci.* **2013**, *447*, 297–305. [CrossRef]
19. Zhang, X.; Motuzas, J.; Liu, S.; da Costa, J.C.D. Zinc-doped BSCF perovskite membranes for oxygen separation. *Sep. Purif. Technol.* **2017**, *189*, 399–404. [CrossRef]
20. Hallberg, P.; Hanning, M.; Rydén, M.; Mattisson, T.; Lyngfelt, A. Investigation of a calcium manganite as oxygen carrier during 99h of operation of chemical-looping combustion in a 10kWth reactor unit. *Int. J. Greenh. Gas Control* **2016**, *53*, 222–229. [CrossRef]
21. Cabello, A.; Abad, A.; Gayán, P.; García-Labiano, F.; de Diego, L.F.; Adánez, J. Increasing energy efficiency in chemical looping combustion of methane by in-situ activation of perovskite-based oxygen carriers. *Appl. Energy* **2021**, *287*, 116557. [CrossRef]
22. Schiestel, T.; Kilgus, M.; Peter, S.; Caspary, K.J.; Wang, H.; Caro, J. Hollow fibre perovskite membranes for oxygen separation. *J. Membr. Sci.* **2005**, *258*, 1–4. [CrossRef]
23. Unger, L.-S.; Ruhl, R.; Meffert, M.; Niedrig, C.; Menesklou, W.; Wagner, S.F.; Gerthsen, D.; Bouwmeester, H.J.M.; Ivers-Tiffée, E. Yttrium doping of $Ba_{0.5}Sr_{0.5}Co_{0.8}Fe_{0.2}O_{3-\delta}$ part II: Influence on oxygen transport and phase stability. *J. Europ. Ceram. Soc.* **2018**, *38*, 2388–2395. [CrossRef]
24. Song, J.; Feng, B.; Chu, Y.; Tan, X.; Gao, J.; Han, N.; Liu, S. One-step thermal processing to prepare $BaCo_{0.95-x}Bi_{0.05}ZrxO_{3-\delta}$ membranes for oxygen separation. *Ceramics Int.* **2019**, *45*, 12579–12585. [CrossRef]

25. Wang, X.; Huang, Y.; Li, D.; Zeng, L.; He, Y.; Boubeche, M.; Luo, H. High oxygen permeation flux of cobalt-free Cu-based ceramic dual-phase membranes. *J. Membr. Sci.* **2021**, *633*, 119403. [CrossRef]
26. He, G.; Baumann, S.; Liang, F.; Hartmann, H.; Jiang, H.; Meulenberg, W.A. Phase stability and oxygen permeability of Fe-based $BaFe_{0.9}Mg_{0.05}X_{0.05}O_3$ (X = Zr, Ce, Ca) membranes for air separation. *Sep. Purif. Technol.* **2019**, *220*, 176–182. [CrossRef]
27. Haworth, P.; Smart, S.; Glasscock, J.; da Costa, J.C.D. High performance yttrium-doped BSCF hollow fibre membranes. *Sep. Purif. Technol.* **2012**, *94*, 16–22. [CrossRef]
28. Tan, X.; Wang, Z.; Meng, B.; Meng, X.; Li, K. Pilot-scale production of oxygen from air using perovskite hollow fibre membranes. *J. Membr. Sci.* **2010**, *352*, 189–196. [CrossRef]
29. Athayde, D.D.; Souza, D.F.; Silva, A.M.A.; Vasconcelos, D.; Nunes, E.H.M.; da Costa, J.C.D.; Vasconcelos, W.L. Review of perovskite ceramic synthesis and membrane preparation methods. *Ceram. Int.* **2016**, *42*, 6555–6571. [CrossRef]
30. Ishii, K.; Matsunaga, C.; Kobayashi, K.; Stevenson, A.J.; Tardivat, C.; Uchikoshi, T. Fabrication of BSCF-based mixed oxide ionic-electronic conducting multi-layered membrane by sequential electrophoretic deposition process. *J. Europ. Ceram. Soc.* **2021**, *41*, 2709–2715. [CrossRef]
31. Baumann, S.; Serra, J.M.; Lobera, M.P.; Escolástico, S.; Schulze-Küppers, F.; Meulenberg, W.A. Ultrahigh oxygen permeation flux through supported $Ba_{0.5}Sr_{0.5}Co_{0.8}Fe_{0.2}O_{3-\delta}$ membranes. *J. Memb. Sci.* **2011**, *377*, 198–205. [CrossRef]
32. Rachadel, P.L.; Souza, D.F.; Nunes, E.H.M.; da Costa, J.C.D.; Vasconcelos, W.L.; Hotza, D. A novel route for manufacturing asymmetric BSCF-based perovskite structures by a combined tape and freeze casting method. *J. Eur. Ceram. Soc.* **2017**, *37*, 5249–5257. [CrossRef]
33. Ding, H.; Luo, C.; Li, X.; Cao, D.; Shen, Q.; Zhang, L. Development of BaSrCo-based perovskite for chemical-looping steam methane reforming: A study on synergistic effects of A-site elements and CeO_2 support. *Fuel* **2019**, *253*, 311–319. [CrossRef]
34. Ramos, A.E.; Maiti, D.; Daza, Y.A.; Kuhn, J.N.; Bhethanabotla, V.R. Co, Fe, and Mn in La-perovskite oxides for low temperature thermochemical CO_2 conversion. *Catal. Today* **2019**, *338*, 52–59. [CrossRef]
35. Shen, Y.; Zhao, K.; He, F.; Li, H. The structure-reactivity relationships of using three-dimensionally ordered macroporous $LaFe_{1-x}Ni_xO_3$ perovskites for chemical-looping steam methane reforming. *J. Energy Inst.* **2019**, *92*, 239–246. [CrossRef]
36. Voorhoeve, R.J.H.; Johnson, D.W.; Remeika, J.P.; Gallagher, P.K. Perovskite Oxides—Materials Science in Catalysis. *Science* **1977**, *195*, 827. [CrossRef]
37. Bhalla, A.S.; Guo, R.; Roy, R. The perovskite structure—A review of its role in ceramic science and technology. *Mater. Res. Innov.* **2000**, *4*, 3–26. [CrossRef]
38. Teraoka, Y.; Zhang, H.M.; Furukawa, S.; Yamazoe, N. Oxygen permeation through perovskite-type oxides. *Chem. Lett.* **1985**, *14*, 1743–1746. [CrossRef]
39. Goldschmidt, V.M. Die gesetze der krystallochemie. *Naturwissenschaften* **1926**, *14*, 477–485. [CrossRef]
40. Yin, Q.; Kniep, J.; Lin, Y.S. Oxygen sorption and desorption properties of Sr-Co-Fe oxide. *Chem. Eng. Sci.* **2008**, *63*, 2211–2218. [CrossRef]
41. Rui, Z.; Ding, J.; Li, Y.; Lin, Y.S. $SrCo_{0.8}Fe_{0.2}O_{3-\delta}$ sorbent for high-temperature production of oxygen-enriched carbon dioxide stream. *Fuel* **2010**, *89*, 1429–1434. [CrossRef]
42. Rui, Z.; Ding, J.; Fang, L.; Lin, Y.S.; Li, Y. $YBaCo_4O_{7+\delta}$ sorbent for oxygen-enriched carbon dioxide stream production at a low-temperature. *Fuel* **2012**, *94*, 191–196. [CrossRef]
43. Schulz, M.; Pippardt, U.; Kiesel, L.; Ritter, K.; Kriegel, R. Oxygen permeation of various archetypes of oxygen membranes based on BSCF. *AIChE J.* **2012**, *58*, 3195–3202. [CrossRef]
44. Leo, A.; Motuzas, J.; Yacou, C.; Liu, S.; Serra, J.M.; Navarrete, L.; Drennan, J.; Julbe, A.; da Costa, J.C.D. Copper oxide—Perovskite mixed matrix membranes delivering very high oxygen fluxes. *J. Membr. Sci.* **2017**, *526*, 323–333. [CrossRef]
45. Motuzas, J.; da Costa, J.C.D. Copper aided exchange in high performance oxygen production by CuCo binary oxides for clean energy delivery. *J. Mater. Chem. A* **2015**, *3*, 17344–17350. [CrossRef]
46. Vieten, J.; Bulfin, B.; Call, F.; Lange, M.; Schmücker, M.; Francke, A.; Roeb, M.; Sattler, C. Perovskite oxides for application in thermochemical air separation and oxygen storage. *J. Mater. Chem. A* **2016**, *4*, 13652–13659. [CrossRef]
47. Zeng, P.; Shao, Z.; Liu, S.; Xu, Z. Influence of M cations on structural, thermal and electrical properties of new oxygen selective membranes based on $SrCo_{0.95}M_{0.05}O_{3-\delta}$ perovskite. *Sep. Purif Technol.* **2009**, *67*, 304–311. [CrossRef]
48. Troncoso, L.; Gardey, M.C.; Fernández-Díaz, M.T.; Alonso, J.A. New rhenium-doped $SrCo_{1-x}Re_xO_{3-\delta}$ perovskites performing as cathodes in solid oxide fuel cells. *Materials* **2016**, *9*, 717. [CrossRef]
49. Li, X.; Kerstiens, T.; Markus, T. Oxygen permeability and phase stability of $Ba_{0.5}Sr_{0.5}Co_{0.8}Fe_{0.2}O_{3-\delta}$ perovskite at intermediate temperatures. *J. Membr. Sci.* **2013**, *438*, 83–89. [CrossRef]
50. Zeng, P.; Chen, Z.; Zhou, W.; Gu, H.; Shao, Z.; Liu, S. Re-evaluation of $Ba_{0.5}Sr_{0.5}Co_{0.8}Fe_{0.2}O_{3-\delta}$ perovskite as oxygen semi-permeable membrane. *J. Membr. Sci.* **2007**, *291*, 148–156. [CrossRef]
51. Carreon, M.A. Porous crystals as membranes. *Science* **2020**, *367*, 624–625. [CrossRef]
52. Ballinger, B.; Motuzas, J.; Smart, S.; da Costa, J.C.D. Palladium cobalt binary doping of molecular sieving silica membranes. *J. Membr. Sci.* **2014**, *453*, 185–191. [CrossRef]
53. Jayaraman, A.; Yang, R.T. Stable oxygen-selective sorbents for air separation. *Chem. Eng. Sci.* **2005**, *60*, 625–634. [CrossRef]
54. Wang, W.; Motuzas, J.; Zhao, X.S.; da Costa, J.C.D. 2D/3D Assemblies of Amine-Functionalized Graphene Silica (Templated) Aerogel for Enhanced CO_2 Sorption. *ACS Appl. Mater. Interfaces* **2019**, *11*, 30391–30400. [CrossRef] [PubMed]

55. Nomura, K.; Ujihira, Y.; Hayakawa, T.; Takehira, K. CO_2 absorption properties and characterization of perovskite oxides, (Ba,Ca)(Co,Fe) $O_{3-\delta}$. *Appl. Catal. A Gen.* **1996**, *137*, 25–36. [CrossRef]
56. Leo, A.; Liu, S.; da Costa, J.C.D. Production of pure oxygen from BSCF hollow fiber membranes using steam sweep. *Sep. Purif. Technol.* **2011**, *78*, 220–227. [CrossRef]
57. Dou, J.; Krzystowczyk, E.; Wang, X.; Richard, A.R.; Robbins, T.; Li, F. $Sr_{1-x}Ca_xFe_{1-y}Co_yO_{3-\delta}$ as facile and tunable oxygen sorbents for chemical looping air separation. *J. Phys. Energy* **2020**, *2*, 025007. [CrossRef]
58. Gokon, N.; Yawata, T.; Bellan, S.; Kodama, T.; Cho, H.-S. Thermochemical behavior of perovskite oxides based on La_xSr_{1-x}(Mn, Fe, Co)$O_{3-\delta}$ and $Ba_ySr_{1-y}CoO_{3-\delta}$ redox system for thermochemical energy storage at high temperatures. *Energy* **2019**, *171*, 971–980. [CrossRef]
59. Fujishiro, F.; Oshima, N.; Sakuragi, T.; Oishi, M. Oxygen desorption properties of perovskite-type $SrFe_{1-x}Co_xO_{3-\delta}$: B-site mixing effect on the reduction properties of Fe and Co ions. *J. Solid State Chem.* **2022**, *312*, 123254. [CrossRef]
60. Zheng, Q.; Lail, M.; Zhou, S.; Chung, C.-C. Novel $CaCo_xZr_{1-x}O_{3-\delta}$ perovskites as oxygen-selective sorbents for air separation. *ChemSusChem* **2019**, *12*, 2598–2604. [CrossRef]